NMR Solution Structure and Backbone Dynamics of the CC Chemokine Eotaxin-3[†,‡]

Jiqing Ye,[§] Kristen L. Mayer, Michael R. Mayer, and Martin J. Stone*

Department of Chemistry, Indiana University, Bloomington, Indiana 47405-0001

Received February 6, 2001; Revised Manuscript Received April 19, 2001

ABSTRACT: Eotaxin-3 is one of three related chemokines that specifically activate chemokine receptor CCR3. We report the 3D structure and backbone dynamics of eotaxin-3 determined by NMR spectroscopy. Eotaxin-3 is monomeric under the conditions in this study and consists of an unstructured N-terminus before the first two conserved cysteine residues, an irregularly structured N-loop following the second conserved cysteine, a single turn of 3_{10}-helix, a three-stranded antiparallel β-sheet, an α-helix, and an unstructured C-terminal tail. As in other chemokines, the α-helix packs against one face of the β-sheet. The average backbone and heavy atom rmsd values of the 20 structures (residues 9−65) are 0.44 and 1.01 Å, respectively. A comparison between the structures of eotaxin-3 and related chemokines suggests that the electrostatic potential in the vicinity of a surface groove and the structure of the $\beta2-\beta3$ turn may be important for maintaining receptor specificity. The backbone dynamics of eotaxin-3 were determined from ^{15}N NMR relaxation data using the extended model free dynamics formalism. Large amplitude motions on the picosecond to nanosecond time scale were observed in both termini and in some residues in the N-loop, the $\beta1-\beta2$ turn, and the β_3 strand; the location of these residues suggests a possible role for dynamics in receptor binding and activation. In contrast to eotaxin, eotaxin-3 exhibits no substantial mobility on the microsecond to millisecond time scale.

A hallmark of tissue inflammation is the accumulation of leukocytes at the inflammatory locus. The migration of leukocytes into tissue in both normal and pathological inflammatory processes is stimulated by small soluble proteins called chemokines (chemotactic cytokines), which activate seven transmembrane helix G protein-coupled receptors located on the leukocyte surface (*1*−*3*). Several chemokine receptors can also function as the coreceptors required by HIV[1] for infection of its target cells (*4*−*8*). Furthermore, recent evidence suggests that chemokine-receptor interactions are critical in controlling the tissue destinations of metastatic cancer cells (*9*). Thus, there is considerable interest in development of agents that will bind to specific chemokine receptors and block HIV infection, cancer metastasis, and/or leukocyte trafficking in inflammatory diseases.

Most of the ∼40 known chemokines can be classified into either of two families, the CC (or β) chemokines, in which the first two of four conserved cysteine residues are contiguous, and the CXC (or α) chemokines, in which the first two cysteine residues are separated by an intervening amino acid. Similarly, most of the ∼17 known chemokine receptors are designated "CCR" or "CXCR", depending whether they are activated by CC or CXC chemokines, respectively (*10*). Generally, the receptors in one family are not responsive to chemokines from the other family. On the other hand, the level of receptor selectivity within each family is much lower (*10*−*12*). Most chemokines can activate multiple receptors, and each receptor is sensitive to several (but not all) chemokines within the relevant family. To date (*2*, *13*), no clear rules have emerged to explain this complex network of chemokine-receptor specificity.

The eotaxin subgroup of CC chemokines, eotaxin/CCL11 (*14*−*16*), eotaxin-2/CCL24 (*17*), and eotaxin-3/CCL26 (*18*), provides an interesting opportunity to probe the molecular determinants of receptor specificity. These chemokines share only 35−41% sequence identity but are all specific agonists for the receptor CCR3. CCR3 is specifically expressed on the surface of eosinophils and basophils. Thus, the eotaxin subgroup chemokines play a role in the trafficking of these cell types, which is relevant to the protection of the gut from parasitic infestation and to allergic and parasitic diseases. The different tissue-specific and stimulus-specific expression patterns of the eotaxin subgroup chemokines suggest that eotaxin, eotaxin-2, and eotaxin-3 are not a case of simple

[†] This work was supported by grants awarded to M.J.S. from the National Institutes of Health (GM 55055 and S10 RR11841), the National Science Foundation (MCB-9600968), and the American Heart Association (Established Investigator Award).

[‡] The coordinates have been deposited with the Protein Data Bank under the accession codes 1G2S and 1G2T.

* To whom correspondence should be addressed. Phone: 812-855-6779. Fax: 812-855-8300. E-mail: mastone@indiana.edu.

[§] Current address: Department of Molecular and Cellular Biology, Harvard University, 7 Divinity Ave., Cambridge, MA 02138.

[1] Abbreviations: 2D and 3D, two and three dimensional; CCR, CC chemokine receptor; CXCR, CXC chemokine receptor; COSY, correlation spectroscopy; DSS, 2,2-dimethyl-2-silapentane-5-sulfonate, sodium salt; HIV, human immunodeficiency virus; HSQC, heteronuclear single-quantum coherence; IL-8, interleukin-8; MCP, monocyte chemoattractant protein; MIP, macrophage inflammatory protein; NMR, nuclear magnetic resonance; NOE, nuclear Overhauser effect; NOESY, nuclear Overhauser effect spectroscopy; rmsd, root-mean-square deviation; RANTES, regulated upon activation normal T-cell expressed and secreted; TOCSY, total correlation spectroscopy; vMIP-II, viral macrophage-inflammatory protein II.

10.1021/bi010252s CCC: $20.00
Published on Web 06/08/2001

redundancy and instead may play complementary roles in the recruitment of eosinophils and basophils (*19*, *20*).

In an attempt to identify structural features of the eotaxin subgroup chemokines that may be important for their receptor specificity, we have undertaken the NMR structure determination of eotaxin-2 and eotaxin-3. The eotaxin-2 structure was reported recently (*21*). Herein, we report the structure and backbone dynamics of eotaxin-3. We also describe a detailed comparison between the structures of the three specific CCR3 agonists (eotaxin, eotaxin-2, and eotaxin-3), two "broad-spectrum" CCR3 agonists (RANTES and MCP-3), the viral CCR3-binding chemokine vMIP-II, and the CC chemokine MCP-1, which shares 65% and 72% sequence identity with eotaxin and MCP-3, respectively, yet does not activate CCR3.

MATERIALS AND METHODS

Gene Synthesis and Cloning. A gene encoding eotaxin-3, with codons optimized for expression in *Escherichia coli*, was synthesized by recursive PCR from eight overlapping oligonucleotides. The PCR product was purified and cloned into the PGEM-T vector (Promega, Madison, WI). The insert was then subcloned into pET28a+ (Novagen, Inc., Madison, WI) between the *Nde*I and *Hin*dIII sites. The recombinant construct (pETX3) encodes a protein which has an N-terminal histidine tag, a factor Xa cleavage site, and the eotaxin-3 sequence. Proteolytic removal of the N-terminal tag by factor Xa is expected to yield eotaxin-3 with a native N-terminus.

Protein Expression and Purification. Eotaxin-3 was overexpressed as inclusion bodies in *E. coli*. BL21(DE3) cells transformed with pETX3 were grown at 37 °C to an OD_{600} of ~0.7−0.8, and expression was induced by the addition of isopropyl β-thiogalactopyranoside (Diagnostic Chemical Limited PEI, Canada) to a final concentration of 1 mM. Cells were harvested 6 h after induction. Expression of uniformly ^{15}N-labeled and ^{15}N,^{13}C-doubled-labeled eotaxin-3 was achieved using isotopically enriched media, as described (*21*, *22*). The cell pellet was suspended in 40 mL of 6 M guanidine hydrochloride, 0.1 M sodium phosphate, and 0.01 M Tris, pH 8.0, per liter of bacteria culture, vortexed for 2 h at room temperature, and then centrifuged (15 000 rpm, 15 min). The supernatant was loaded onto a Ni−NTA−agarose affinity column (Qiagen, Valencia, CA) equilibrated with 8 M urea, 0.1 M sodium phosphate, and 0.01 M Tris, pH 8. The column was washed with the same buffer at pH 6, and then the recombinant protein was eluted with the same buffer at pH 4. The eluted protein was diluted to ~150 μg/mL in eluting buffer and treated with DTT (5 mM) at room temperature for 1 h. The recombinant protein was then refolded by dialyzing against 50 mM Tris, 50 mM glycine, 0.5 M NaCl, 3 M urea, 4 mM reduced glutathione, 0.4 mM oxidized glutathione, and 0.02% NaN_3, pH 8 for 24 h, then against 50 mM Tris, 50 mM glycine, 0.5 M NaCl, 1 M urea, 2.5 mM reduced glutathione, 0.5 mM oxidized glutathione, and 0.02% NaN_3, pH 8 for 24 h, and finally against 50 mM Tris, 0.1 M NaCl, and 2 mM $CaCl_2$, pH 8. The protein was concentrated to ~1 mg/mL and cleaved by factor Xa (New England Biolabs, Inc., Beverly, MA; 1 μg/ 400 μg of fusion protein) at room temperature overnight. The mature protein was further purified on a HR10/10 15S cation-exchange chromatography column (Pharmacia Biotech, Piscataway, NJ) using a 0−2 M NaCl gradient. Eotaxin-3 eluted as the major peak at ~0.7 M NaCl. Mass spectrometry of the purified protein showed the molecular weight was as expected. The yield of purified eotaxin-3 was ~10 mg/L of culture. Eotaxin and eotaxin-2 were expressed and purified as described previously (*21*, *23*).

Competitive Radioligand Binding Assay. The binding of eotaxin, eotaxin-2, and eotaxin-3 to CCR3 was assayed using a competitive radioligand binding assay performed using previously reported procedures with slight modifications (*18*). The murine L1.2 pre-B cell line stably transfected with CCR3 (*18*) was obtained as a gift from Dr. Osamu Yoshi and was maintained in RPMI 1640, 10% fetal bovine serum, and 0.8 mg/mL geneticin; all cell culture materials were purchased from Gibco-BRL (Rockville, MD). A total of 4×10^6 L1.2-CCR3 cells/mL in 25 mM HEPES, 1 mM $CaCl_2$, 5 mM $MgCl_2$, 120 mM NaCl, and 0.5% bovine serum albumin (protease free, Sigma, Milwaukee, WI), pH 7.6, was incubated with approximately 0.15 nM [^{125}I]eotaxin (~2000 Ci/mmol, Amersham Pharmacia Biotech) and increasing amounts of cold competitor protein in 250 μL for 1 h at room temperature. After the incubation period, the cells were layered onto an ice-cold sucrose cushion [20% sucrose, 140 mM NaCl, 40 mM Tris, 0.4% bovine serum albumin (protease free, Sigma, Milwaukee, WI), pH 7.6] and centrifuged for 10 min at 1500*g*. Both liquid layers were carefully aspirated, the cells were resuspended in scintillation fluid, and radioactivity was counted on a Packard 1600 TR liquid scintillation counter. The data were fit to the equation percent inhibition $= (B_{max}[L])/(IC_{50} + [L])$, in which B_{max} is the maximum binding, [L] is the cold competitor concentration, and IC_{50} is the midpoint of the transition. All binding assays were performed in duplicate.

NMR Spectroscopy. Eotaxin-3 samples for NMR were ~2 mM protein in 20 mM deuterated sodium acetate and 0.02% NaN_3, pH 5.0. All NMR experiments were performed at 303 K on a Varian UnityINOVA 500 MHz spectrometer with a triple-resonance three-axis gradient probe. Proton chemical shifts were referenced to external DSS (0 ppm). ^{15}N and ^{13}C chemical shifts were referenced indirectly to liquid ammonia and tetramethylsilane, respectively (*24*). All NMR data were processed on a Silicon Graphics workstation using Felix98 (Molecular Simulations Inc., San Diego, CA). Experimental details for NMR experiments are listed in the Supporting Information.

NMR spectra for backbone resonance assignments included ^{1}H−^{15}N HSQC, CBCA(CO)NH, HNCACB, HBHA(CBCACO)NH, and HNCA. Aliphatic side-chain assignments were achieved using ^{15}N-edited TOCSY-HSQC, HCCTOCSY-(CO)NH, CC-TOCSY-(CO)NH, and HCCH-TOCSY; the ^{1}H and ^{13}C isotropic mixing times were 50 and 15−20 ms, respectively. The aromatic resonances were assigned using a 3D aromatic HCCH-TOCSY, a 2D (HB)CB(CGCD)HD, NOEs to β protons, and NOEs among aromatic protons. Side-chain amide protons of asparagines and glutamines were assigned on the basis of NOEs to β and γ protons. Stereospecific assignments of the isopropyl methyl groups of valines and leucines were obtained using a ^{13}C-edited nonconstant time HSQC collected on a 10% ^{13}C-labeled sample in D_2O (*25*). Stereospecific assignments of β-methylene protons of five residues (C10, S26, C50, Y61, and L64)

were made on the basis of $^3J_{H\alpha H\beta}$ values and NOEs between the β-methylene protons and the amide protons in a ^{15}N-edited NOESY-HSQC with a mixing time of 50 ms.

Distance and Dihedral Angle Restraints. Distance restraints were obtained from 3D ^{13}C-separated NOESY-HSQC (sample in D_2O), 3D ^{15}N-separated NOESY-HSQC, and ^{15}N/^{13}C simultaneously separated NOESY-HSQC spectra (sample in 90% H_2O/10% D_2O); mixing times were 150 ms. NOE restraints were classified as strong (1.8−2.7 Å), medium (1.8−3.3 Å), or weak (1.8−5.0 Å) on the basis of the cross-peak volumes, calibrated using intraresidue NOEs and short-range NOEs in well-characterized secondary structure elements (*26*). A total of 1, 1.5, and 2 Å were added to the respective upper bounds for restraints involving nonstereospecifically assigned methylene protons, stereospecifically assigned methyl groups, and aromatic protons.

Backbone ϕ angle restraints were obtained on the basis of the $^3J_{HNH\alpha}$ coupling constants determined from a 3D HNHA experiment. The ϕ angles were constrained to $-60° \pm 30°$ for $^3J_{HNH\alpha} < 5.5$ Hz, $-120° \pm 60°$ for $^3J_{HNH\alpha} > 7$ Hz, $-120° \pm 50°$ for $^3J_{HNH\alpha} > 8$ Hz, $-120° \pm 40°$ for $^3J_{HNH\alpha} > 9$ Hz, and $-100° \pm 80°$ if the $^3J_{HNH\alpha}$ constant was between 6 and 7 Hz and the intraresidue $H_\alpha-H_N$ NOE was weaker than the sequential $H_\alpha-H_N$ NOE (*27*). Side-chain χ_1 angles were constrained on the basis of the $^3J_{H\alpha H\beta}$ constants, determined from a 3D HACAHB-COSY (*28*) spectrum, and NOE patterns (*21*, *29*). If both $^3J_{H\alpha H\beta}$ coupling constants were <5 Hz, the side-chain χ_1 angle was constrained to $60° \pm 60°$. If one of the two $^3J_{H\alpha H\beta}$ constants was >10 Hz, the χ_1 angle was constrained to either $-60° \pm 60°$ or $180° \pm 60°$ (distinguished on the basis of NOEs) or to $-120° \pm 120°$ (if the two possible conformations could not be distinguished) (*30*).

Slowly exchanging protons were identified as those with observable signals in an ~14 min ^{1}H−^{15}N HSQC spectrum initiated ~4 min after the lyophilized protonated protein was dissolved in D_2O buffer. A hydrogen bond restraint involving a slowly exchanging proton was added if a consistent hydrogen-bonding partner was observed in at least one-third of the initial structures inspected (*21*).

Structure Calculations. Structure calculations were performed on a Silicon Graphics O_2 workstation using a hybrid distance geometry-simulated annealing protocol implemented in X-PLOR (*31*, *32*), as described previously (*21*, *32*). A family of 20 structures was selected on the basis of energies, NOE violations, dihedral angle violations, and the $\phi-\varphi$ angle pairs in Ramachandran space evaluated by X-PLOR and AQUA/PROCHECK (*33*). The average structure was calculated and refined by heating to 1000 K and gradually cooling back to 100 K over 6000 steps (3 fs/step), followed by 200 steps of restrained energy minimization. The coordinates and input constraints have been deposited in the Protein Data Bank (*34*); accession codes are 1G2T for the ensemble of 20 structures and 1G2S for the energy-minimized average structure.

^{15}N Relaxation and Backbone Dynamics. ^{15}N longitudinal (R_1) and transverse (R_2) relaxation rates, heteronuclear {^{1}H}−^{15}N NOEs, and transverse cross-relaxation rates (η_{xy}) for 62 residues were measured using 2D ^{1}H−^{15}N correlation pulse sequences and nonlinear curve fitting, as described (*22*, *35*). Estimation of the components of the molecular rotational diffusion tensor was performed using the coordinates of the energy-minimized average structure of eotaxin-3 as described (*22*, *36*); 12 residues (G3, S4, D5, I6, S7, K8, T9, K17, T67, K69, Q70, and L71) were excluded from the diffusion tensor calculation on the basis of large-amplitude fast internal motions (NOE < 0.5), and 11 residues (C11, F12, Y14, T22, N32, S35, R45, T51, H52, R54, and K56) were excluded because their R_2/η_{xy} values exceeded the average R_2/η_{xy} value (1.66) by more than one standard deviation (0.13), indicating that their R_2 values may be affected by slow conformational exchange. The R_2/R_1 values of the remaining 39 residues were fit to isotropic, axially symmetric, and fully anisotropic diffusion models. *F*-statistical tests suggested that the data should ideally be fit using the fully anisotropic model. However, to facilitate implementation of data fitting using the program Modelfree 4.0, we chose to use an oblate axially symmetric diffusion tensor. This choice is reasonable because the two largest diffusion tensor components obtained from the fully anisotropic model are similar (D_{zz}:D_{xx}:D_{yy} = 1.31:1.20:1) and the fit to an oblate tensor is better than that to a prolate model (χ^2 = 156.2 versus 175.8). The relaxation parameters were fit to the Lipari−Szabo model-free dynamics formalism (*37*) or extended versions thereof (*38*), as described (*22*, *36*, *39*).

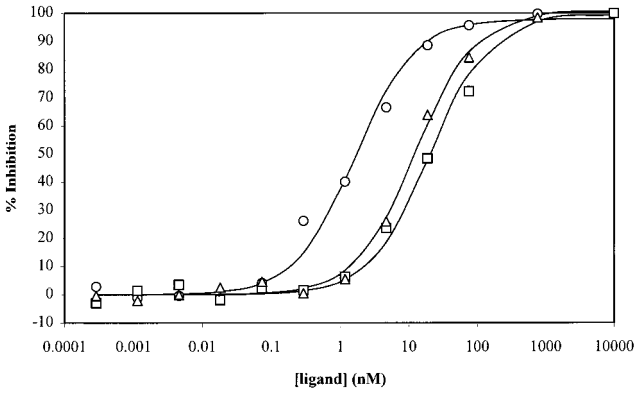

FIGURE 1: Competitive radioligand binding data for eotaxin (circles), eotaxin-2 (squares), and eotaxin-3 (triangles). Experimental details are given in Materials and Methods.

RESULTS

Eotaxin-3 Expression and Receptor Binding. Eotaxin-3 was expressed in *E. coli* as inclusion bodies, refolded, and purified as described in Materials and Methods. The ability of eotaxin-3 to bind to CCR3 was determined using a competitive radioligand binding assay (Figure 1). The concentration of cold eotaxin-3 required for half-maximal inhibition of hot eotaxin binding (IC_{50}) was 12 ± 2 nM, as compared to IC_{50} values of 1.6 ± 0.3 nM for eotaxin and 20 ± 3 nM for eotaxin-2. The IC_{50} values for eotaxin-3 and eotaxin are the same within error as those reported previously (*18*); the IC_{50} for eotaxin-2 has not been published previously.

Resonance Assignments, Geometrical Restraints, and Secondary Structure. Almost complete NMR resonance assignments for recombinant eotaxin-3 were obtained using the experiments described in Materials and Methods and the Supporting Information. The NH group assignments are shown on the HSQC spectrum in Figure 2. The backbone amide resonances of R2 and H16 were missing, presumably due to extremely fast exchange with H_2O or line-broadening effects resulting from intermediate time scale conformational

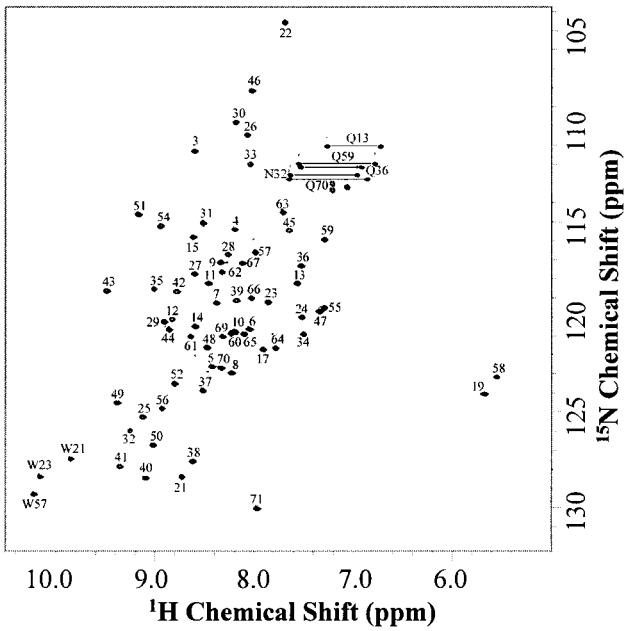

FIGURE 2: ^{1}H−^{15}N HSQC spectrum and amide resonance assignments. Each backbone cross-peak in the ^{1}H−^{15}N HSQC spectrum of eotaxin-3 was assigned, and the corresponding residue number is shown near the cross-peak. The side-chain amide groups of tryptophans (W21, W23, W57), glutamines (Q13, Q36, Q59, Q70), and asparagine (N32) were also assigned.

Table 1: Summary of Restraints

distance restraints (total 1157)	
intraresidue ($i - j = 0$)	441
sequential ($\|i - j\| = 1$)	260
short range ($\|i - j\| \leq 4$)	155
long range ($\|i - j\| > 4$)	301
dihedral restraints (total 69)	
ϕ	53
χ_1	16
hydrogen bonds	17 × 2
total restraints	1250
total restraints per residue	17.6
total restraints per residue (9−65)	20.5

exchange. Notably, the amide proton resonances of L19 (5.67 ppm) and V58 (5.55 ppm) and the H_α resonances of P18 (2.39 ppm), V24 (3.51 ppm), and V58 (2.86 ppm) were significantly shifted upfield.

The geometric restraints used for the structure calculations are summarized in Table 1 and Figure 3A. These included 1157 distance restraints, of which 301 were from long-range NOEs, and 69 dihedral angle restraints. Eighteen slowly exchanging amide protons were identified from the H−D exchange experiment, and 17 hydrogen bonds were introduced after the hydrogen-bonding partners were consistently identified in the initial structures. The average number of restraints was 17.6 for all residues and 20.5 for residues 9−65. On the bais of the distributions of short- and medium-range NOEs, the $^{3}J_{HNH\alpha}$ values, the slowly exchanging amide protons, and the deviations of C_α, C_β, and H_α chemical shifts from random coil values, it was possible to predict the positions of three β-strands and two helical regions as indicated in Figure 4 (*26*, *40*, *41*). In addition, cross-strand NOEs and patterns of slowly exchanging amide protons indicated that the β-strands assemble into an antiparallel β-sheet with the second strand sandwiched between the other two strands.

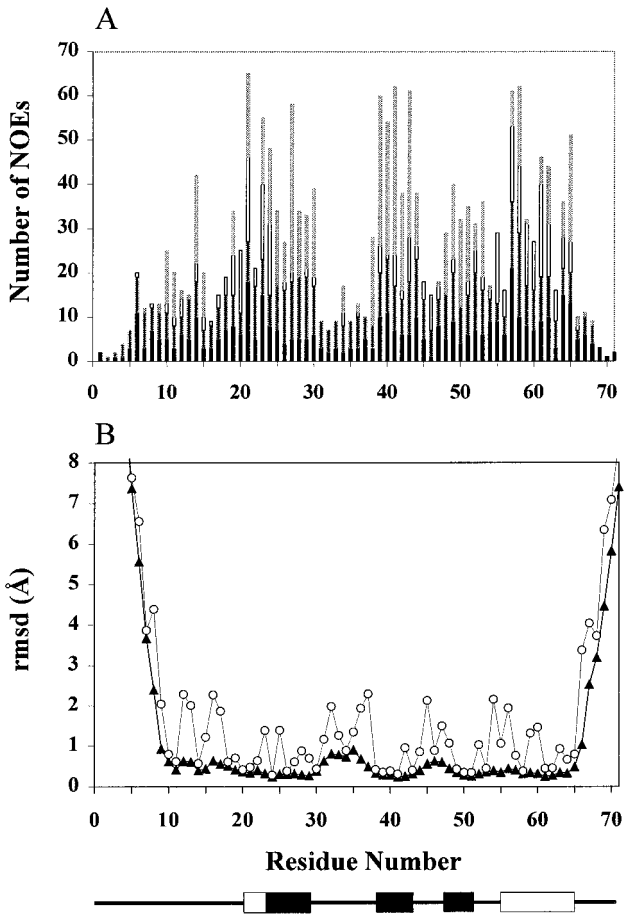

FIGURE 3: (A) Number of NOE restraints per residue. The NOE restraints for each residue are categorized as intraresidue ($i = j$), sequential ($|i - j| = 1$), short-range (($|i - j| \leq 4$), and long-range NOEs ($|i - j| > 4$); i and j are the residue numbers where the two NOE-forming protons reside. Intraresidue, sequential, short-range, and long-range NOEs are represented by solid bars, horizontal stripes, open bars, and gray bars, respectively, from the bottom to the top of each stacked column. (B) Average backbone heavy atom (▲) and all heavy atom (○) rmsd values for the family of 20 structures relative to the average structure. The positions of the secondary structure elements of eotaxin-3 are indicated at the bottom as filled bars (β-strands) or open bars (turn of 3_{10}-helix or C-terminal α-helix).

Three-Dimensional Structures. Eotaxin-3 was found to exist as a monomer under the conditions of this study on the basis of the following evidence: (1) all NOEs were consistent with a monomeric structure; (2) analysis of relaxation data (see below) indicated an apparent molecular correlation time of 5.07 ± 0.01 ns, similar to those for other monomeric chemokines (*22*, *42*−*45*); (3) the N-terminal region, which is involved in dimerization of some CC chemokines, was not protected from H−D exchange, exhibited exchange cross-peaks with water in ^{15}N-edited NOESY-HSQC and TOCSY-HSQC spectra, and showed low heteronuclear NOEs, indicating that it was highly flexible; and (4) equilibrium sedimentation for samples of 12−200 μM eotaxin-3 indicated an apparent molecular mass close to the monomer mass (data not shown). Therefore, structure calculations were performed for the monomeric eotaxin-3 species.

Structural statistics for the 20 selected output structures and the energy-minimized average structure of eotaxin-3 are listed in Table 2. For the family of 20 structures, the

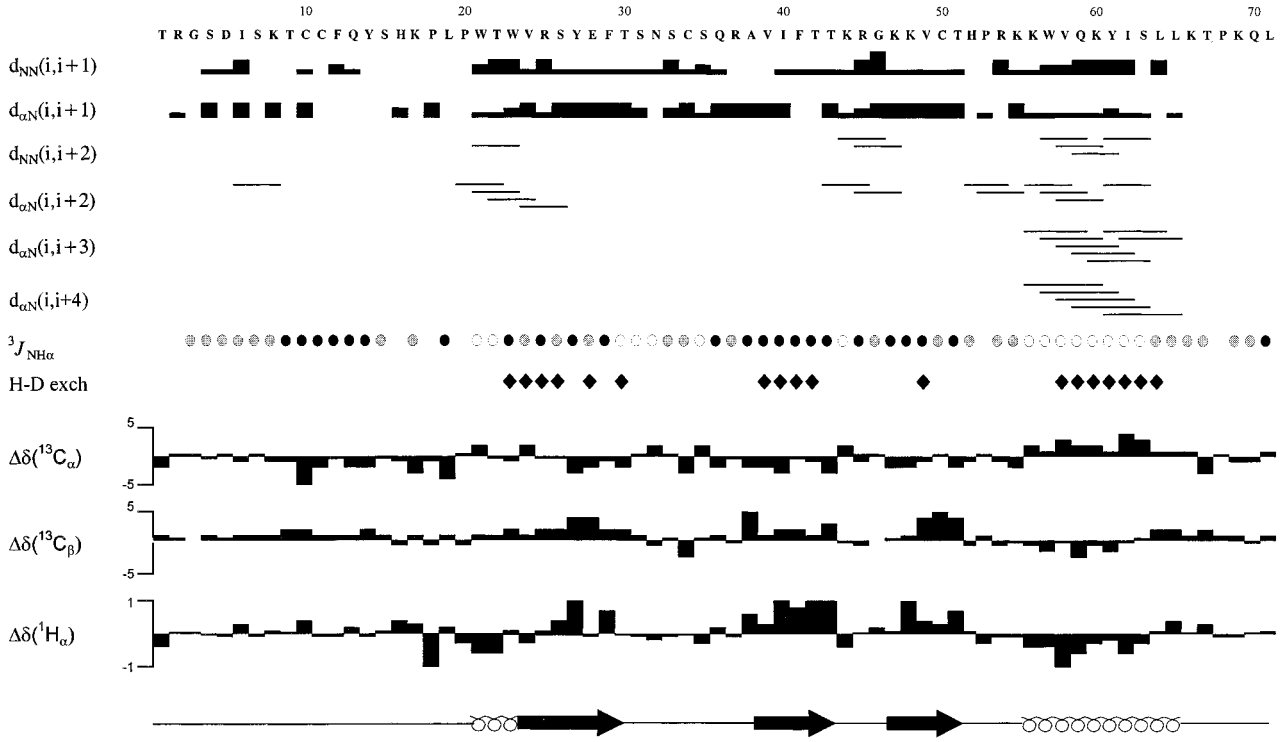

FIGURE 4: Summary of the NMR data for the secondary structure determination of eotaxin-3. The amino acid sequence of eotaxin-3 is shown at the top. The sequential and medium-range NOEs are indicated by bars and lines, respectively. The relative strength of the sequential NOEs is indicated by the thickness of the bars. The $^3J_{HNH\alpha}$ coupling constants of 57 residues, obtained from an HNHA spectrum, are classified as follows: >8 Hz, solid circles; 6−8 Hz, shaded circles; and <6 Hz, open circles. The slowly exchanging protons are indicated by filled diamonds. The deviations of the chemical shifts of C_α, C_β, and H_α from the random coil values are shown in the histograms. The positions of the two helical regions and the three β-strands deduced from the data are indicated at the bottom.

Table 2: Results of Structure Calculations

	⟨eotaxin-3⟩[a]	eotaxin-3 min[b]
rmsd from ideal geometry		
bonds (Å)	0.0019 ± 0.0001	0.0018
angles (deg)	0.523 ± 0.004	0.510
impropers (deg)	0.375 ± 0.007	0.3589
rmsd from experimental restraints		
distance (Å)	0.011 ± 0.001	0.010
dihdedral angle (deg)	0.078 ± 0.036	0.057
NOE violations per structure		
>0.15 Å	0	0
>0.1 Å	0.9	0
dihedral violations per structure		
>1	0	0
>0.5	0.9	0
X-PLOR energies (kcal mol^{-1})		
overall	119.8 ± 2.0	112.5
bond lengths	4.4 ± 0.3	4.1
bond angles	91.7 ± 1.4	87.2
impropers	13.9 ± 4.9	12.8
van der Waals	2.5 ± 0.4	2.8
NOE	7.3 ± 0.7	5.4
dihedral	0.03 ± 0.03	0.01
Ramachandran analysis (residue 9−65)		
most favored regions (%)	74.2	77.4
additional allowed regions (%)	24.7	22.6
generously allowed regions (%)	1.0	0.0
disallowed regions (%)	0.0	0.0
rmsd from mean structure (Å) (backbone/heavy atoms)		
all residues	1.66/2.31	
residues 9−65	0.44/1.01	
residues 9−30, 38−65	0.40/0.94	

[a] Family of 20 structures. [b] Energy-minimized average structure.

interproton distances and dihedral angles agree closely with the input restraints, and the deviations of geometrical parameters from ideal values are small. The backbone conformations of the well-ordered residues (9−65) are energetically favored with 99% of the $\phi-\varphi$ angle pairs in the most favored or additionally allowed regions of the Ramachandran map. The backbone and all heavy atom rmsd values of each residue are plotted in Figure 3B. Both the N-terminal and the C-terminal regions are poorly defined with large rmsd values, but the average rmsd values of residues 9−65 are low (0.44 and 1.01 Å for backbone atoms and all heavy atoms, respectively); if the 30s loop (residues 31−37) is excluded, the rmsd values decrease further to 0.40 and 0.94 Å, respectively. The energy-minimized average structure also agrees closely with the experimental data and ideal geometry (Table 2).

The family of 20 structures and the energy-minimized average structure of eotaxin-3 are shown in parts A and B of Figure 5, respectively. The main features of the structure are an unstructured N-terminus (residues 1−9) before the first two conserved cysteines, an irregularly structured region (the N-loop, residues 12−20) following the second conserved cysteine, a single turn of 3_{10}-helix (residues 21−23), a three-stranded antiparallel β-sheet (β1, residues 25−29; β2, residues 39−43; and β3, residues 47−51), and a C-terminal α-helix (residues 56−65). The β1 strand contains a β-bulge (R25, S26, and T42 as positions 1, 2, and X, respectively) which closely resembles a classic bulge except that the φ angle of position 2 is distorted (−153.5° versus 160° for a classic bulge). In the 30s loop (residues 30−38), which connects the β1 and β2 strands, the amide proton of T30 forms a hydrogen bond with the backbone carbonyl of A38, and the amide proton of A38 forms a hydrogen bond with the side-chain hydroxyl of T30. The 30s loop is relatively poorly defined as indicated by the rmsd values. The β2 and

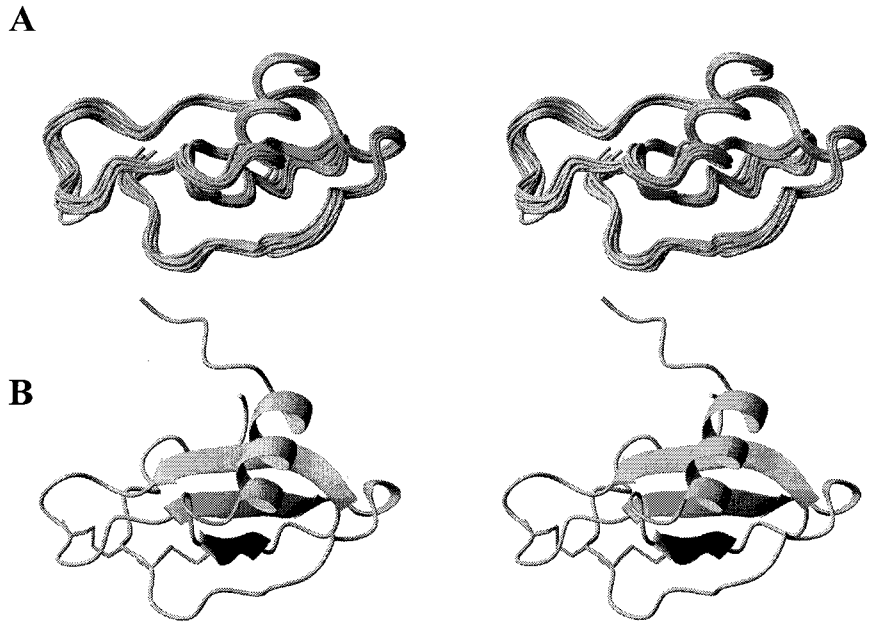

FIGURE 5: Structures of eotaxin-3. (A) Stereoview of the family of 20 structures. The structures are represented by C_α traces of the well-ordered region (residues 9−65). (B) Ribbon representation of the average energy-minimized structure of the full-length eotaxin-3 (residues 1−71). Disulfide bonds are shown in thin lines. Both (A) and (B) were prepared using the program MOLMOL (*68*).

β3 strands are connected by a type I/III turn with T43, L44, R45, and G46 as positions 1−4, respectively. A type III turn with H52, P53, R54, and K55 as positions 1−4 connects the β3 strand and the C-terminal α-helix. The C-terminus, from residue 66 to residue 71, is also disordered, as indicated by large rmsd values (Figure 3B).

The C-terminal α-helix of eotaxin-3 lies across one side of the β-sheet, making extensive hydrophobic interactions with the β-sheet. Hydrophobic residues on one side of the α-helix (W57, V58, Y61, I62, and L65) make contacts with V49 and T51 in the β3 strand, V39 and F41 in the β2 strand, and Y27 and S26 in the β1 strand. In addition, L19 from the N-loop, W23 from the helical turn, V24 preceding the β1 strand, and T43 from the second β-strand make hydrophobic contacts with each other and with side chains from the α-helix. The aforementioned upfield shifts of V58 and L19 H_N resonances and P18, V24, and V58 H_α resonances can be understood by the positions of these protons above or below the aromatic rings of W21 and W57. Analogous upfield shifts of L19 and V58 (or their equivalents) have been observed in other chemokines (*21*, *46*−*48*). Indeed, residues involved in the hydrophobic interactions are highly conserved among chemokines.

The N-terminus and the N-loop are tethered to the core structure through two disulfide bonds, which are almost completely conserved in the chemokine superfamily. The C11−C50 disulfide is well defined with an average (±standard deviation) χ_3 angle of $-67° \pm 10°$, consistent with the left-handed spiral seen in other chemokines (*21*, *49*). The C10−C34 disulfide is less well defined; 16 of the final 20 structures have χ_3 angles of $-84° \pm 10°$ (i.e., left-handed), whereas the remaining four structures have χ_3 angles ranging from 60° to 150°.

The N-loop is wrapped around the edge of the β3 strand with segments on both sides of the β-sheet. The N-terminus and part of the N-loop (residues 12−14) are packed against the side of the β-sheet opposite to the α-helix, whereas the remainder of the N-loop (residues 15−20) and the helical turn are packed against the same side of the sheet as the C-terminal α-helix. NOEs were observed from S7 and T9 in the N-terminus to I40 in the β2 strand; T9 also showed NOEs to T30 and C34 in the 30s loop. The side chains of F12 and Q13 (on one side of the sheet) and H16 and K17 (on the other side) are largely exposed to solvent without much contact to other residues. However, Y14 and S15 are buried, making extensive contact with V49, C50, and T51 in the β3 strand. The side chains of Y14 and S15 are on opposite sides of the β3 strand, resembling a clamp that may help to tether the N-loop to the core structure. This suggestion is consistent with the heavy atom rmsd values of F12, Q13, H16, and K17 being higher than those of Y14 and S15 (Figure 3B).

Backbone Dynamics. Several regions of the eotaxin-3 structural ensemble are noticeably less ordered than the secondary structural core. In addition, previous studies have suggested that dynamic flexibility may play a role in receptor recognition by chemokines (*22*, *42*). Therefore, we investigated the dynamics of the eotaxin-3 backbone by analysis of ^{15}N relaxation data according to the Lipari−Szabo model-free formalism. Relaxation data (R_1, R_2, NOE, and η_{xy}) were obtained for all non-proline residues except R2 and H16, which did not appear in the HSQC spectrum, and C10 and K60, which were overlapped; these data and the R_2/R_1 and R_2/η_{xy} ratios are shown in Figure 6A−F.

The internal dynamics parameters were obtained by fitting the relaxation data (R_1, R_2, and NOE) of each residue to one of five models describing internal motions (*39*). Data for only one residue (H52) were accounted for by the simplified Lipari−Szabo formalism (effective internal correlation time, $\tau_e \leq 20$ ps), whereas data for 42 residues were described by a model with $20 < \tau_e < 500$ ps. Data for 10 residues (W21, T22, V24, C34, S35, Q36, K47, T51, R54, and K55) required the additional incorporation of a small R_{ex} term (= 1.2 s) to account for conformational rearrangements on the micro-

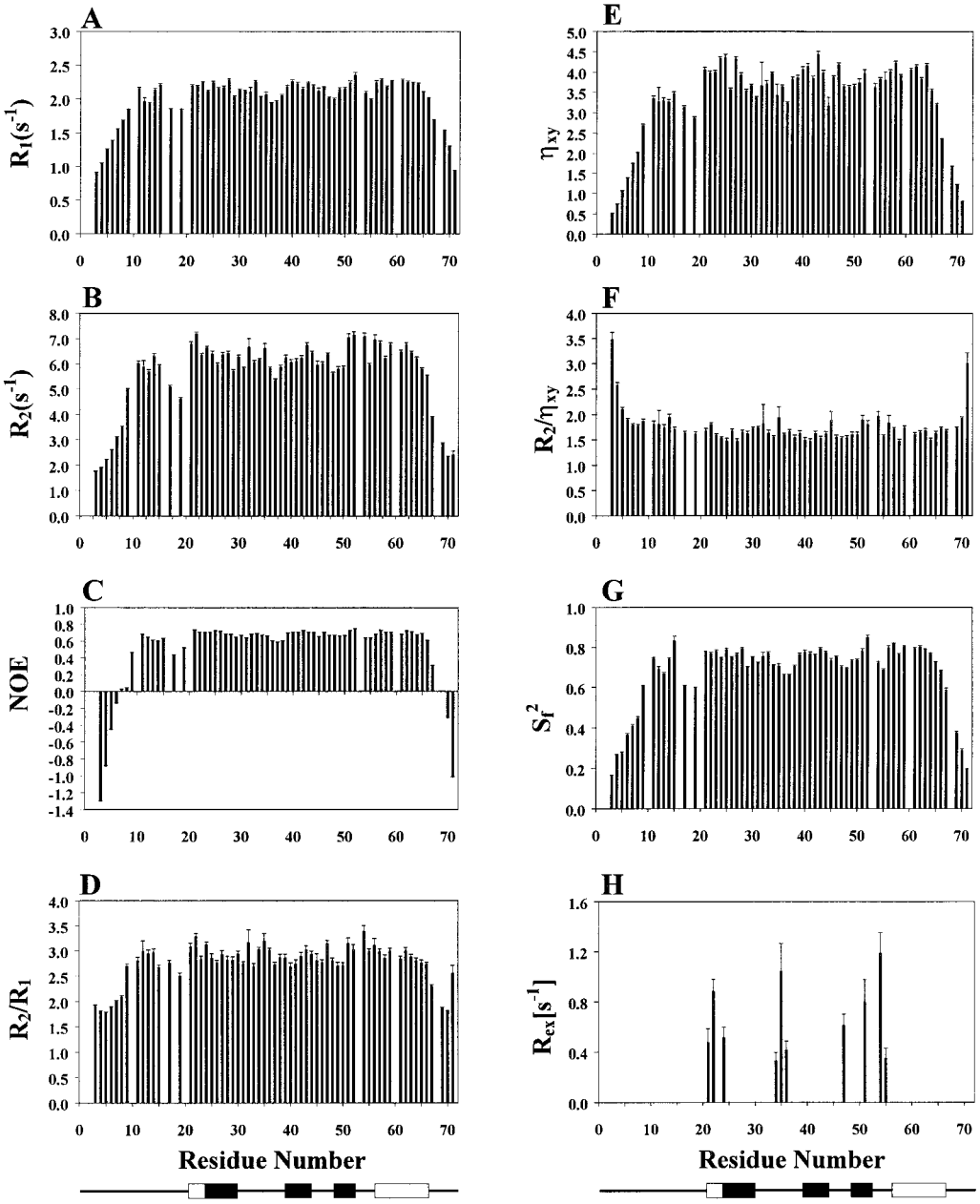

FIGURE 6: Plots of the relaxation parameters and the model-free dynamics parameters. (A) R_1, (B) R_2, (C) $\{^1H\}-^{15}N$ NOE, (D) R_2/R_1, (E) η_{xy}, (F) R_2/η_{xy}, (G) S_f^2, and (H) R_{ex} are plotted against the residue number. The positions of the secondary elements of eotaxin-3 are indicated at the bottom of each column as in Figure 3.

second to millisecond time scale or possibly deviations from the axially symmetric molecular diffusion model. Finally, nine residues (S4, D5, I6, S7, K8, S15, T67, K69, Q70) could only be fit adequately by a model involving two time scales of internal motion faster than the molecular tumbling; all of these except S15 (see below) are in the extended termini, suggesting segmental motions of these regions. The final optimization of the diffusion tensor yielded an effective molecular rotational correlation time (τ_m) of 5.07 ± 0.01 ns with $D_{\|}/D_{\perp} = 0.88 \pm 0.02$; the unique axis of the diffusion tensor is oriented parallel to the vector connecting the C_α atoms of residues Phe-29 and Lys-48. The relaxation and dynamics parameters are listed in the Supporting Information.

The order parameters S^2, describing the amplitude of the fast time scale internal motion, are shown in Figure 6G. The average generalized order parameter is 0.66 ± 0.20 for all residues whereas the average for the core secondary structure (β1, β2, β3, and the C-terminal α-helix) is 0.76 ± 0.03. Figure 7 shows the eotaxin-3 structure color coded according to the fast time scale order parameter (S_f^2). In general, residues in the termini, loops, and turns are more flexible than those in the core secondary structures. The generalized order parameters for both termini range from 0.17 to 0.68, which is significantly lower than the range for residues in the core secondary structures. Several other residues also have lower order parameters including F12, Q13, K17, and L19 in the N-loop, Q36 and R37 in the 30s loop, K47 and K48 in the β3 strand, and K55 in the turn connecting the β3 strand and the α-helix. As shown in Figure 6A−C, the more extensive high-frequency motions of these residues are generally evident in the raw relaxation data by lower than average R_1, R_2, and NOE values.

The R_{ex} terms for the 10 residues fit to the extended Lipari−Szabo formalism are plotted in Figure 6H. The values

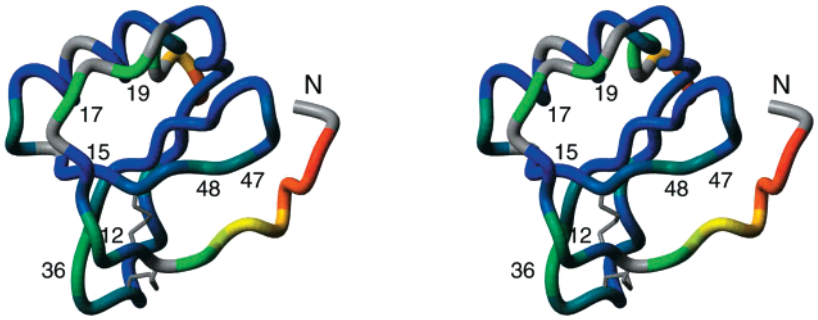

FIGURE 7: Stereoview of the backbone C_α traces of eotaxin-3 color coded according to the values of the order parameters (S_f^2). Residues are colored in a continuous spectrum from red to blue, with red corresponding to the most flexible and blue to the most rigid regions. The color scale is red ($S_f^2 \leq 0.2$), yellow ($S_f^2 = 0.40$), green ($S_f^2 = 0.60$), and blue ($S_f^2 \geq 0.80$). Those residues whose relaxation data were not available due to spectral overlap are colored in gray. The side chains of the four conserved cysteine residues and the two disulfide bonds are shown as gray cylinders. This figure was prepared using the coordinates of the average minimized NMR structures in the program MOLMOL (*68*).

```
                  10        20        30        40        50        60        70
EOTAXIN-3  TRGSDISKTCCFQYSHKPLPWTWVRSYEF-TSNSCSQRAVIFTTKRGKKVCTHPRKKWVQKYISLLKTPKQL
EOTAXIN     GPASVPTTCCFNLANRKIPLQRLESYRRITSGKCPQKAVIFKTKLAKDICADPKKKWVQDSMKYLDQKSPTPKP
EOTAXIN-2     VVIPSPCCMFFVSKRIPENRVVSYQLSSRSTCLKAGVIFTTKKGQQFCGDPKQEWVQRYMKNLDAKQKKASPR
RANTES     SPYSSDTTPCCFAYIARPLPRAHIKEYFY-TSGKCSNPAVVFVTRKNRQVCANPEKKWVREYINSLEMS
MCP-3     QPVGINTSTTCCYRFINKKIPKQRLESYRRTTSSHCPREAVIFKTKLDKEICADPTQKWVQDFMKHLDKKTQTPKL
MCP-4     QPDALNVPSTCCFTFSSKKISLQRLKSYVI-TTSRCPQKAVIFRTKLGKEICADPKEKWVQNYMKHLGRKAHTLKT
vMIP-II    LGASHRPDKCCLGYQKRPLPQVLLSSWYP-TSQLCSKPGVIFLTKRGRQVCADKSKDWVKKLMQQLPVTAR
MCP-1     QPDAINAPVTCCYNFTNRKISVQRLASYRRITSSKCPKEAVIFKTIVAKEICADPKQKWVQDSMDHLDKQTQTPKT
                  10        20        30        40        50        60        70
```

FIGURE 8: Sequence alignment of the CCR3 ligands eotaxin-3, eotaxin, eotaxin-2, RANTES, MCP-3, MCP-4, and vMIP-II and the CCR2 ligand MCP-1. Numbering at the top corresponds to eotaxin-3 and numbering at the bottom corresponds to MCP-1. The conserved cysteine residues are in bold type. Residues that are unique in MCP-1 are shaded. Underlined residues in eotaxin-3 have S^2 values more than one standard deviation below the average for secondary structure elements ($S^2 < 0.73$).

range from 0.35 to 1.2 s^{-1}. Notably, R_2/η_{xy} values for the four residues with the highest R_{ex} values ($R_{ex} > 0.70$ s^{-1} for T22, S35, T51, and R54) are all at least one standard deviation higher than the average value for the core secondary structure residues, indicating that these R_{ex} terms are likely to result from slow conformational exchange. The smaller R_{ex} terms for the remaining six residues could potentially result from either true conformational exchange, more complex molecular diffusion than is accounted for by the axially symmetric model, or a data-fitting artifact.

DISCUSSION

CCR3 Recognition by CC Chemokines. With the structure of eotaxin-3 reported here, structures have now been determined for six CC-chemokine agonists of the receptor CCR3, namely, eotaxin, eotaxin-2, eotaxin-3, RANTES, MCP-3, and vMIP-II (*46*−*51*); note that vMIP-II has been reported by different groups to be a CCR3 agonist or an antagonist (*52*, *53*). In addition, both NMR and X-ray structures have been reported for MCP-1, which shares 65% and 72% sequence identity with eotaxin and MCP-3, respectively, yet binds to CCR3 ~600-fold more weakly than eotaxin and does not activate CCR3 (*54*). These 3D structures provide an opportunity to explore the structural features that may be required for CCR3 recognition. Thus, we searched for aspects of the structures that are shared by the six high-affinity CCR3 ligands but differ in MCP-1.

First, it is noteworthy that MCP-1 and RANTES are dimeric under conditions of structure determination whereas the other CCR3 ligands are all monomers. RANTES dimerizes through its N-terminus, in a manner similar to MIP-1β (*48*, *51*, *55*), whereas MCP-1 can dimerize either through the N-terminal region or through the first β-strand, similar to IL-8 (*49*, *56*, *57*). Although there has been extensive interest in the role of dimerization in chemokine activity, the preponderance of the current evidence is that the monomeric form is active, as discussed previously (*49*). Thus, we focus here on structural differences at the monomer level.

A sequence alignment for the six high-affinity CCR3 ligands and MCP-1 is presented in Figure 8, and the overlaid backbone structures are shown in Figure 9. The three β-strands and the α-helix superimpose well for all structures whereas the N-loop follows the same general path with slightly increased variation between structures. The N- and C-termini show essentially no correlation between structures, as expected from their high rmsd values in each structural family and their high flexibility indicated by relaxation data. Initial observation of these structures does not reveal any individual structural feature of the MCP-1 backbone that differs dramatically from all of the CCR3 ligands. A quantitative comparison of the pairwise similarities (rmsd values) between the secondary structure regions of these seven chemokines is presented in Table 3, along with pairwise sequence identities and sequence similarities. The rmsd values (of the three β-strands and the α-helix) among the CCR3 ligands range from 0.68 to 1.39 Å, whereas the rmsd values between MCP-1 and the CCR3 ligands range from 0.81 to 1.23 Å, within the variations among the CCR3 ligands. Furthermore, there is no clear correlation between the pairwise rmsd values and the percent sequence identities. For example, MCP-1 and MCP-3 share 72% sequence identity, yet the rmsd between them is 1.15 Å, whereas

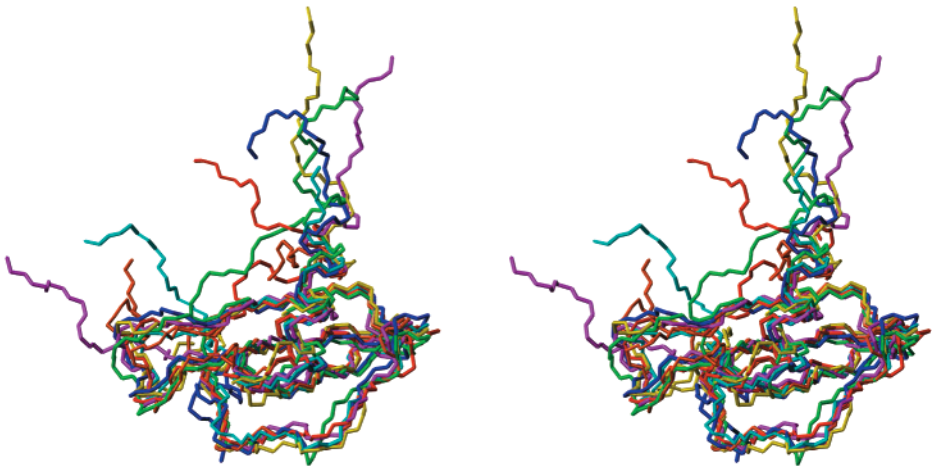

FIGURE 9: Stereoview of the average energy-minimized structures (backbone traces) of eotaxin (blue), eotaxin-2 (green), RANTES (cyan), MCP-3 (yellow), vMIP-II (orange), and MCP-1 (magenta) overlaid onto eotaxin-3 (red). The superposition was performed by minimizing the deviation between residues 10−65 of eotaxin-3 and the corresponding residues in each other chemokine. The PDB accession codes for these protein structures are listed in the footnote to Table 3.

Table 3: Sequence Identities and Similarities and Pairwise rmsd Values for CC Chemokines[a]

	eotaxin-3	eotaxin	eotaxin-2	RANTES	MCP-3	vMIP-II	MCP-1
eotaxin-3	**0.45**	41, 20	35, 25	40, 26	28, 21	38, 21	31, 24
eotaxin	0.94	**0.39**	38, 22	40, 24	65, 16	32, 16	65, 18
eotaxin-2	1.35	0.87	**0.42**	26, 30	39, 25	31, 22	35, 20
RANTES	0.96	0.68	1.03	**0.61**	31, 37	38, 26	30, 31
MCP-3	0.81	1.26	1.39	0.91	**N/A**	28, 27	72, 8
vMIP-II	1.04	0.85	1.03	0.88	1.04	**0.38**	28, 22
MCP-1	0.89	0.81	1.23	1.12	1.15	0.91	**0.48**

[a] The upper right half of the table shows the percentage sequence identity followed by the percentage sequence similarity between each pair of chemokines. The diagonal entries (boldfaced) are the rmsd values for each family of structures; the structural ensemble is not available for MCP-3. The lower left half of the table shows the rmsd values resulting from best fit superpositions of the β-sheets and the C-terminal α-helices in the energy-minimized average structures of each pair of chemokines, i.e., residues 25−29, 39−43, 47−51, and 56−65 for eotaxin-3 and the corresponding residues for the other chemokines. PDB accession codes for eotaxin, eotaxin-2, eotaxin-3, RANTES, vMIP-II, and MCP-1 are 2eot, 1eih, 1g2s, 1rtn, 1hfn, and 1don for structural ensembles and 1eot, 1eig, 1g2t, 1rto, 1hfg, and 1dom for energy-minimized average structures, respectively. The energy-minimized average structure of MCP-3 was from PDB file 1bo0.

eotaxin-3 and MCP-3 share 28% sequence identity with an rmsd of 0.81 Å.

To further search for differences between the backbone structures of MCP-1 and the CCR3 ligands, we performed a distance difference analysis (*58*). In this approach, the C_α to C_α distances were measured for each pair of residues in each chemokine. The average and standard deviation of the analogous distances in the six CCR3 ligands were calculated and compared to the corresponding distance in MCP-1. Residue pairs whose separation in MCP-1 is more than two standard deviations different from the average for the other chemokines are indicated in Figure 10. The following features are apparent. First, distances between the N-terminal region and several other structural elements are significantly increased in MCP-1 whereas those from the N-terminus to the 30s loop are significantly decreased (box A, Figure 10). This reflects the fact that the N-terminus of MCP-1 (which is involved in dimerization) extends away from the center of the β-sheet and toward the 30s loop. Considering that the N-termini of chemokines are flexible, this average structural difference may not be physiologically relevant. Second, distances from residues in the helical turn to the N-loop, all three β-strands, and the central residues of the α-helix and interresidue distances among residues 20−30 (helical turn and β1 strand) are significantly shorter in MCP-1 (region labeled B in Figure 10). These observations reflect the lack of a β-bulge at the beginning of the β1 strand, resulting in tighter packing of the helical turn in MCP-1. Third, distances within the β2−β3 hairpin and from the β2−β3 turn and β2 strand to the 30s loop are also shorter in MCP-1 than in the other chemokines (box C, Figure 10). This is of a consequence of the tighter β2−β3 turn structure in MCP-1, which may contribute to receptor specificity (see below). Fourth, the N-loop is closer to the β2−β3 region in MCP-1 than in the other chemokines (box D, Figure 10), apparently due to a movement of the N-loop upward (as depicted in Figure 9). The N-loops of chemokines are known to participate in receptor binding. However, the importance of a subtle change in the average structure of the N-loop is unclear due to the relatively high dynamic flexibility of the loop. Finally, residues 63−65 in the α-helix are closer to the helical turn and the β2−β3 turn than in the other chemokines (box E, Figure 10), as illustrated by the slight shift of the MCP-1 helix to the right (see Figure 9) relative to the other proteins. We have previously proposed that the N-terminal part of the helix may participate in receptor binding (*21*), so this subtle shift could potentially affect specificity. Although these few structural elements clearly show systematic shifts in MCP-1 compared to the CCR3 ligands, it is important to note that the structural changes are quite subtle in all cases.

The chemokines eotaxin, eotaxin-2, MCP-1, IL-8, and fractalkine all bind to peptides derived from the N-terminus of their respective receptors (*21*, *23*, *44*, *59*−*61*). Chemical

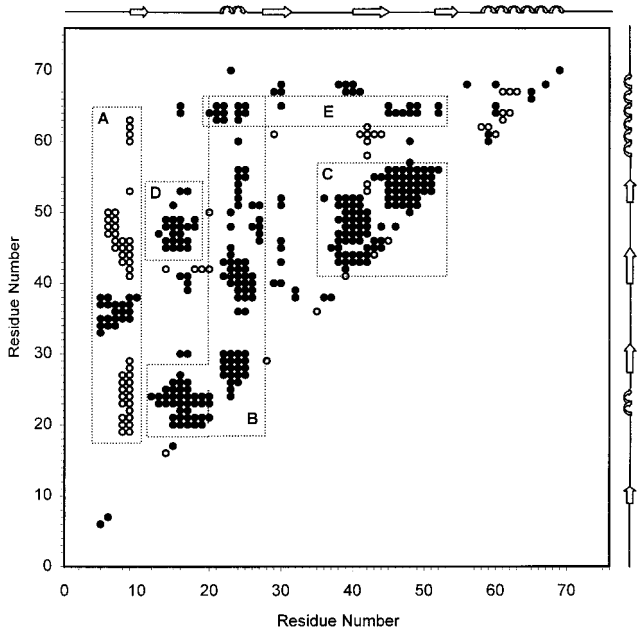

FIGURE 10: Plot showing the C_α to C_α distances in MCP-1 that are more than two standard deviations different from the average corresponding distance in the six CCR3 ligands: eotaxin, eotaxin-2, eotaxin-3, RANTES, MCP-3, and vMIP-II. Distances that increase and decrease in MCP-1 relative to the other chemokines are represented as open and closed circles, respectively. The regions labeled A−E are discussed in the text. The positions of the secondary structure elements are indicated schematically at the top and right.

shift changes (and calculated structures in the case of IL-8) indicate that the peptide binds into a shallow extended groove whose edges are formed by residues from the N-loop and the $\beta2-\beta3$ hairpin of the chemokine. The base of the groove is hydrophobic whereas its edges are polar. We have suggested previously that the specificity difference between MCP-1 and the CCR3 agonists may be due to a difference in the surface electrostatic potential of these chemokines in the vicinity of this binding groove (*21*). This proposal was based on comparisons of eotaxin, eotaxin-2, and MCP-1. We have now extended this comparison to include the structure of eotaxin-3 reported here as well as MCP-3, RANTES, and vMIP-II. The electrostatic potential of the binding groove is substantially more positive for all of the high-affinity CCR3 ligands than it is for MCP-1 (not shown). To investigate the source of this difference, we have searched for residues in MCP-1 that differ from the corresponding residues in the six CCR3 ligands listed above and from those in MCP-4, a CCR3 agonist whose 3D structure has not been reported. Nine such residues were identified: Ala-7, Val-9, Thr-16, Val-22, Ala-26, Ile-46, Val-47, Asp-65, and Gln-70; these are shaded in the sequence alignment in Figure 8. Hemmerich et al. have shown that mutation of Val-9 or Ile-46 does not influence CCR2 binding by MCP-1 (*59*); mutations at the other positions were not investigated. One of these residues, Ile-46, which is located in the $\beta2-\beta3$ turn and at one end of the proposed binding groove, is replaced by a positively charged residue (Lys or Arg) in all seven CCR3 ligands. The following residue, Val-47, is also replaced by Lys or Arg in four of the CCR3 ligands. Considering that the $\beta2-\beta3$ hairpin of MCP-1 was one of the regions identified above to have a systematic structural difference from the other chemokines, that this region of MCP-1 lacks the positive charges found in the CCR3 ligands, and that this region helps to define the putative receptor-binding groove, the $\beta2-\beta3$ turn is clearly a strong candidate for a receptor specificity determinant. Two other residues of MCP-1 may also contribute to the difference in surface electrostatic potential. Asp-65 and Gln-70 are each replaced by lysine in eotaxin, eotaxin-2, MCP-3, and MCP-4 and by a neutral residue in eotaxin-3, RANTES, and vMIP-II. Gln-70 is located near the C-terminus and seems unlikely to play a significant role in receptor specificity. Asp-65 is located in the central part of the α-helix. On the basis of NMR chemical shift changes upon receptor peptide binding, we have proposed that the CCR3 N-terminus extends from the groove and wraps around the surface of eotaxin-2 contacting some residues on the α-helix (*21*). If this is true, the replacement of a positively charged or neutral residue by Asp-65 may decrease the affinity for CCR3. Again, the subtle structural change noted above for this region of the helix may act in concert with the change in electrostatic potential.

Possible Role of Dynamics in Chemokine Activity. The ^{15}N relaxation data described here yield information about the flexibility of the eotaxin-3 backbone on a fast (picosecond to nanosecond) time scale and a slower (microsecond to millisecond) time scale. Similar analyses have been reported for several other chemokines, including eotaxin, vMIP-II, IL-8, and fractalkine (*22*, *42*−*44*, *62*). The eotaxin-3 data revealed that several regions of the structure have substantial flexibility on the picosecond to nanosecond time scale. The N- and C-termini are highly flexible, as observed for all other chemokines and in line with the high rmsd values in this region of the structure. In addition, residues in the N-loop, the 30S loop, and the $\beta3$ strand exhibit slightly larger amplitudes of picosecond to nanosecond motion (lower order parameters) than the majority of residues.

In the N-loop, the order parameters (S_f^2) of F12, N13, K17, and L19 are at least one standard deviation below the average of the regular structure regions (0.76) whereas the order parameter of Y14 ($S_f^2 = 0.74$) is comparable to the average of the regular structure regions. Residue S15 also has a higher S_f^2 value (0.83), but the double time scale Lipari−Szabo model ($S_s^2 = 0.81$ and $\tau_e = 1.5$ ns) is required to adequately fit the relaxation data for this residue. These observations indicate that the motion of the N-loop is restricted in the middle (residues 14 and 15) but has much more substantial high-frequency motions at each end. These results correlate well with the rmsd values in the family of structures; backbone rmsd values are 0.40 and 0.44 Å for residues 14 and 15, respectively, but 0.59 ± 0.05 Å for residues 12−13 and 16−18. Furthermore, a similar variation of both order parameters and rmsd values was observed for eotaxin (*22*, *46*), and the rmsd values of eotaxin-2 also vary similarly (*21*). This trend can be understood from the fact that the N-loop of eotaxin crosses the $\beta3$ strand with the side chains of residues Y14 and S15 packing directly against opposite sides of the β-sheet, whereas the residues located nearer the ends of the N-loop do not interact directly with the sheet and have few long-range NOEs. Mutational studies have shown that residues corresponding to F12 and K17 of eotaxin-3 are important for receptor binding and activation in eotaxin, MCP-1, and RANTES (*59*, *63*, *64*). Thus, it is tempting to speculate that the flexibility of these regions may be necessary to allow them to sample a large conformational

space and establish contacts with the receptor. The possible importance of conformational flexibility in receptor binding is further suggested by the locations of other regions exhibiting large-amplitude fast internal motions. K47 and K48, in the β3 strand, are situated on one edge of the putative receptor-binding groove. Also, 30s loop residues Q35 and R36, while not directly contributing to the binding groove, are adjacent to F12 in the tertiary structure. In addition, there is extensive mutational evidence for the importance of the highly flexible N-termini of chemokines in receptor recognition (*49*, *65*−*67*). Finally, the C-terminus exhibits extensive high-frequency motions that are unlikely to be of functional significance. Notably, the regions identified by distance difference analysis or sequence comparisons as most likely contributing to receptor specificity do not have unusually low order parameters. Thus, these regions may serve as "anchor" points for the receptor interaction with the intervening regions being more conformationally flexible.

In a previous study of the backbone dynamics of eotaxin, we observed that residues adjacent to the two conserved disulfide bonds undergo slow (microsecond to millisecond time scale) internal motions, as indicated by R_{ex} terms and the broadening or absence of resonances in the NMR spectra. Relaxation studies of vMIP-II (*43*) and eotaxin-2 (K. L. Mayer and M. J. Stone, unpublished results) have also revealed evidence for slow motions near the disulfide bonds. We speculated that such motion might be a common feature of CC chemokines and might potentially be required for induced fit to the receptor (*22*). The current results indicate that the R_{ex} terms for eotaxin-3 are extremely small (<1.2 s^{-1} compared to as much as 7.4 s^{-1} for eotaxin) and that they are not localized to the vicinity of the disulfide bonds. Although the absence of a large R_{ex} term for a specific residue does not necessarily indicate the absence of slow motions for that residue, it would be surprising if extensive microsecond to millisecond time scale motions were present without any residue exhibiting a significant R_{ex} value. The only evidence suggesting slow motions in eotaxin-3 is that the resonances of His-16 are missing in the ^{15}N HSQC spectrum and weak (presumably broadened) in ^{13}C-edited spectra. However, since His-16 is not adjacent to the disulfide bonds and the residues neighboring His-16 do not show any evidence for slow motions, we can conclude that the nature and distribution of slow motions in eotaxin-3 are quite different from those in eotaxin. Thus, it appears less likely that slow time scale motions are directly linked to receptor binding or activation.

Concluding Remarks. The solution structure of eotaxin-3 reported here is very similar to those of other high-affinity CCR3 ligands including eotaxin, eotaxin-2, MCP-3, RANTES, and vMIP-II. However, the following significant differences exist between these structures and that of MCP-1, a low-affinity CCR3 antagonist. (1) The electrostatic potentials at the proposed receptor-binding surfaces of the CCR3 ligands are significantly more positive than that of MCP-1. The lower electrostatic potential in MCP-1 may result from the lack of positively charged residues in the positions of Ile-46 and Val-47 (Lys-44 and Arg-45, respectively, in eotaxin-3) and from the negatively charged residue Asp-65 (Lys-63 in eotaxin-3). (2) The turn between the β2 and β3 strands, which helps to define the putative receptor-binding groove, is tighter in MCP-1 than in the other chemokines. (3) The N-terminal half of the α-helix, which may interact with the receptor N-terminus, is shifted slightly in MCP-1. ^{15}N relaxation data for eotaxin-3 indicate the presence of large-amplitude fast internal motions for N-loop and β3 strand residues that line the putative binding groove. Considering that receptor activation is believed to involve a conformational rearrangement of the receptor, these data suggest that optimal interaction of chemokines and their receptors may involve structural reorganization of both binding partners. Thus, chemokine-receptor binding may be a case of mutual induced fit.

ACKNOWLEDGMENT

The authors thank Drs. Lewis E. Kay, Mark A. Rance, and Arthur G. Palmer, III, for providing NMR and data analysis software. We also thank Drs. Mark D. Pagel and Ulrike Werner-Zwanziger for technical assistance.

SUPPORTING INFORMATION AVAILABLE

A table summarizing the details of NMR data collection and a table listing the relaxation and dynamics parameters for eotaxin-3. This material is available free of charge via the Internet at http://pubs.acs.org.

REFERENCES

1. Chensue, S. W., and Ward, P. A. (1996) in *Anderson's Pathology* (Damjanov, I., Ed.) pp 387−415, Mosby-Year Book, Inc., St. Louis, MO.
2. Baggiolini, M., Dewald, B., and Moser, B. (1997) *Annu. Rev. Immunol. 15*, 675−705.
3. Luster, A. D. (1998) *N. Engl. J. Med. 338*, 436−445.
4. Feng, Y., Broder, C. C., Kennedy, P. E., and Berger, E. A. (1996) *Science 272*, 872−877.
5. Berger, E. A., Murphy, P. M., and Farber, J. M. (1999) *Annu. Rev. Immunol. 17*, 657−700.
6. Wells, T. N. C., Proudfoot, A. E., Power, C. A., and Marsh, M. (1996) *Chem. Biol. 3*, 603−609.
7. Ward, S. G., and Westwick, J. (1998) *Biochem. J. 333*, 457−470.
8. Doms, R. W., and Peiper, S. C. (1997) *Virology 235*, 179−190.
9. Muller, A., Homey, B., Soto, H., Ge, N., Catron, D., Buchanan, M. E., McClanahan, T., Murphy, E., Yuan, W., Wagner, S. N., Barrera, J. L., Mohar, A., Verastegui, E., and Zlotnik, A. (2001) *Nature 410*, 50−56.
10. Zlotnik, A., and Yoshie, O. (2000) *Immunity 12*, 121−127.
11. Murphy, P. M. (1994) *Annu. Rev. Immunol. 12*, 593−633.
12. Murphy, P. M. (1996) *Cytokine Growth Factor Rev. 7*, 47−64.
13. Rollins, B. (2000) *Blood 90*, 909−928.
14. Garcia-Zepeda, E. A., Rothenberg, M. E., Ownbey, R. T., Celestin, J., Leder, P., and Luster, A. D. (1997) *Nat. Med. 2*, 449−456.
15. Kitaura, M., Nakajima, T., Imai, T., Harada, S., Combadiere, C., Tiffany, H. L., Murphy, P. M., and Yoshie, O. (1996) *J. Biol. Chem. 271*, 7725−7730.
16. Ponath, P. D., Qin, S. X., Ringler, D. J., Clarklewis, I., Wang, J., Kassam, N., Smith, H., Shi, X. J., Gonzalo, J. A., Newman, W., Gutierrezramos, J. C., and Mackay, C. R. (1996) *J. Clin. Invest. 97*, 604−612.
17. Forssmann, U., Uguccioni, M., Loetscher, P., Dahinden, C. A., Langen, H., Thelen, M., and Baggiolini, M. (1997) *J. Exp. Med. 185*, 2171−2176.
18. Kitaura, M., Suzuki, N., Imai, T., Takagi, S., Suzuki, R., Nakajima, T., Hirai, K., Nomiyama, H., and Yoshie, O. (1999) *J Biol. Chem. 274*, 27975−27980.

19. Shinkai, A., Yoshisue, H., Koike, M., Shoji, E., Nakagawa, S., Saito, A., Takeda, T., Imabeppu, S., Kato, Y., Hanai, N., Anazawa, H., Kuga, T., and Nishi, T. (1999) *J. Immunol. 163*, 1602−1610.
20. Roebuck, K. A., Carpenter, L. R., Lakshminarayanan, V., Page, S. M., Moy, J. N., and Thomas, L. L. (1999) *J. Leukocyte Biol. 65*, 291−298.
21. Mayer, K. L., and Stone, M. J. (2000) *Biochemistry 39*, 8382−8395.
22. Ye, J., Mayer, K. L., and Stone, M. J. (1999) *J. Biomol. NMR 15*, 115−124.
23. Ye, J., Kohli, L. L., and Stone, M. J. (2000) *J. Biol. Chem. 275*, 27250−27257.
24. Wishart, D. S., Bigam, C. G., Yao, J., Abildgaard, F., Dyson, H. J., Oldfield, E., Markley, J. L., and Sykes, B. D. (1995) *J. Biomol. NMR 6*, 135−140.
25. Neri, D., Szyperski, T., Otting, G., Senn, H., and Wuthrich, K. (1989) *Biochemistry 28*, 7510−7516.
26. Wuthrich, K. (1986) *NMR of Proteins and Nucleic Acids* Wiley, New York.
27. Clubb, R. T., Ferguson, S. B., Walsh, C. T., and Wagner, G. (1994) *Biochemistry 33*, 2761−2772.
28. Grzesiek, S., Kuboniwa, H., Hinck, A. P., and Bax, A. (1995) *J. Am. Chem. Soc. 117*, 5312−5315.
29. Kraulis, J., Clore, G. M., Nilges, M., Jones, T. A., Pettersson, G., Knowles, J., and Gronenborn, A. M. (1989) *Biochemistry 28*, 7241−7257.
30. Barsukov, I. L., and Luan, L. Y. (1993) in *NMR of Macromolecules: a practical approach* (Roberts, G. C. K., Ed.) pp 315−355, Oxford University Press Inc., New York.
31. Nilges, M., Clore, G. M., and Gronenborn, A. M. (1988) *FEBS Lett. 229*, 317−324.
32. Brunger, A. T. (1993) *X-PLOR Version 3.1, A System for X-ray Crystallography and NMR*, Yale University Press, New Haven, CT.
33. Laskowski, R. A., Rullmannn, J. A., MacArthur, M. W., Kaptein, R., and Thornton, J. M. (1996) *J Biomol. NMR 8*, 477−486.
34. Berman, H. M., Westbrook, J., Feng, Z., Gilliland, G., Bhat, T. N., Weissig, H., Shindyalov, I. N., and Bourne, P. E. (2000) *Nucleic Acids Res. 28*, 235−242.
35. Kroenke, C. D., Loria, J. P., Lee, L. K., Rance, M., and Palmer, A. G. (1998) *J. Am. Chem. Soc. 120*, 7905−7915.
36. Seewald, M. J., Pichumani, K., Stowell, C., Tibbals, B. V., Regan, L., and Stone, M. J. (2000) *Protein Sci. 9*, 1177−1193.
37. Lipari, G., and Szabo, A. (1982) *J. Am. Chem. Soc. 104*, 4559−4570.
38. Barbato, G., Ikura, M., Kay, L. E., Pastor, R. W., and Bax, A. (1992) *Biochemistry 31*, 5269−5278.
39. Mandel, A. M., Akke, M., and Palmer, A. G., III (1995) *J. Mol. Biol. 246*, 144−163.
40. Wishart, D. S., Sykes, B. D., and Richards, F. M. (1992) *Biochemistry 31*, 1647−1651.
41. Wishart, D. S., and Sykes, B. D. (1994) *J. Biomol. NMR 4*, 171−180.
42. Crump, M. P., Spyracopoulos, L., Lavigne, P., Kim, K. S., Clark-Lewis, I., and Sykes, B. D. (1999) *Protein Sci. 8*, 2041−2054.
43. LiWang, A. C., Cao, J. J., Zheng, H., Lu, Z., Peiper, S. C., and LiWang, P. J. (1999) *Biochemistry 38*, 442−453.
44. Mizoue, L. S., Bazan, J. F., Johnson, E. C., and Handel, T. M. (1999) *Biochemistry 38*, 1402−1414.
45. Lawrence, J. S., LiWang, A. C., and LiWang, P. J. (1998) *Biochemistry 37*, 9346−9354.
46. Crump, M. P., Rajarathnam, K., Kim, K. S., Clark-Lewis, I., and Sykes, B. D. (1998) *J. Biol. Chem. 273*, 22471−22479.
47. Kim, K. S., Rajarathnam, K., Clarklewis, I., and Sykes, B. D. (1996) *FEBS Lett. 395*, 277−282.
48. Chung, C. W., Cooke, R. M., Proudfoot, A. E. I., and Wells, T. N. C. (1995) *Biochemistry 34*, 9307−9314.
49. Stone, M. J., and Mayer, K. L. (1999) in *Chemokines in Allergic Disease* (Rothenberg, M. E., Ed.) pp 67−94, Marcel Dekker, New York.
50. LiWang, A. C., Wang, Z. X., Sun, Y., Peiper, S. C., and LiWang, P. J. (1999) *Protein Sci. 8*, 2270−2280.
51. Skelton, N. J., Aspiras, F., Ogez, J., and Schall, T. J. (1995) *Biochemistry 34*, 5329−5342.
52. Boshoff, C., Endo, Y., Collins, P. D., Takeuchi, Y., Reeves, J. D., Schweickart, V. L., Siani, M. A., Sasaki, T., Williams, T. J., Gray, P. W., Moore, P. S., Chang, Y., and Weiss, R. A. (1997) *Science 278*, 290−294.
53. Kledal, T. N., Rosenkilde, M. M., Coulin, F., Simmons, G., Johnsen, A. H., Alouani, S., Power, C. A., Luttichau, H. R., Gerstoft, J., Clapham, P. R., Clark-Lewis, I., Wells, T. N. C., and Schwartz, T. W. (1997) *Science 277*, 1656−1659.
54. Daugherty, B. L., Siciliano, S. J., Demartino, J. A., Malkowitz, L., Sirotina, A., and Springer, M. S. (1996) *J. Exp. Med. 183*, 2349−2354.
55. Lodi, P. J., Garrett, D. S., Kuszewski, J., Tsang, M. L. S., Weatherbee, J. A., Leonard, W. J., Gronenborn, A. M., and Clore, G. M. (1994) *Science 263*, 1762−1767.
56. Handel, T. M., and Domaille, P. J. (1996) *Biochemistry 35*, 6569−6584.
57. Lubkowski, J., Bujacz, G., Boque, L., Domaille, P. J., Handel, T. M., and Wlodawer, A. (1997) *Nat. Struct. Biol. 4*, 64−69.
58. Nelson, M. R., and Chazin, W. J. (1998) *Protein Sci. 7*, 270−282.
59. Hemmerich, S., Paavola, C., Bloom, A., Bhakta, S., Freedman, R., Grunberger, D., Krstenansky, J., Lee, S., McCarley, D., Mulkins, M., Wong, B., Pease, J., Mizoue, L., Mirzadegan, T., Polsky, I., Thompson, K., Handel, T. M., and Jarnagin, K. (1999) *Biochemistry 38*, 13013−13025.
60. Clubb, R. T., Omichinski, J. G., Clore, G. M., and Gronenborn, A. M. (1994) *FEBS Lett. 338*, 93−97.
61. Skelton, N. J., Quan, C., Reilly, D., and Lowman, H. (1999) *Struct. Folding Des. 7*, 157−168.
62. Grasberger, B. L., Gronenborn, A. M., and Clore, G. M. (1993) *J. Mol. Biol. 230*, 364−372.
63. Pakianathan, D. R., Kuta, E. G., Artis, D. R., Skelton, N. J., and Hebert, C. A. (1997) *Biochemistry 36*, 9642−9648.
64. Mayer, M. R., and Stone, M. J. (2001) *J. Biol. Chem.* (in press).
65. Crump, M. P., Gong, J. H., Loetscher, P., Rajarathnam, K., Amara, A., Arenzana-Seisdedos, F., Virelizier, J. L., Baggiolini, M., Sykes, B. D., and Clark-Lewis, I. (1997) *EMBO J. 16*, 6996−7007.
66. Gong, J.-H., and Clark-Lewis, I. (1995) *J. Exp. Med. 181*, 631−640.
67. Strieter, R. M., Polverini, P. J., Kunkel, S. L., Arenberg, D. A., Burdick, M. D., Kasper, J., Dzuiba, J., Vandamme, J., Walz, A., Marriott, D., Chan, S. Y., Roczniak, S., and Shanafelt, A. B. (1995) *J. Biol. Chem. 270*, 27348−27357.
68. Koradi, R., Billeter, M., and Wüthrich, K. (1996) *J. Mol. Graphics 14*, 51−55.

BI010252S